Nanoscale

PAPER

View Article Online
View Journal | View Issue

Cite this: *Nanoscale*, 2015, **7**, 19620

Synthesis and electrochemical properties of spherical and hollow-structured NiO aggregates created by combining the Kirkendall effect and Ostwald ripening†

Jung Sang Cho, Jong Min Won, Jong-Heun Lee and Yun Chan Kang*

Received 31st August 2015,
Accepted 19th October 2015

DOI: 10.1039/c5nr05930e

www.rsc.org/nanoscale

The Kirkendall effect and Ostwald ripening were successfully combined to prepare uniquely structured NiO aggregates. In particular, a NiO–C composite powder was first prepared using a one-pot spray pyrolysis, which was followed by a two-step post-treatment process. This resulted in the formation of micron-sized spherical and hollow-structured NiO aggregates through a synergetic effect that occurred between nanoscale Kirkendall diffusion and Ostwald ripening. The discharge capacity of the spherical and hollow-structured NiO aggregates at the 500th cycle was 1118 mA h g^{-1} and their capacity retention, which was measured from the second cycle, was nearly 100%. However, the discharge capacities of the solid NiO aggregates and hollow NiO shells were 631 and 150 mA h g^{-1}, respectively, at the 500th cycle and their capacity retentions, which were measured from the second cycle, were 63 and 14%, respectively. As such, the spherical and hollow-structured NiO aggregates, which were formed through the synergetic effect of nanoscale Kirkendall diffusion and Ostwald ripening, have high structural stability during cycling and have excellent lithium storage properties.

Introduction

Thin-walled, hollow nanopowders have been widely studied due to their unique nanoscale properties and their applicability to various fields, including energy storage, gas sensors, catalysts, and magnetic and biomedical applications.[1–17] These hollow nanopowders can be prepared through the use of both organic and inorganic templates.[12,13,18–21] In recent years, conversion chemical reactions have been successfully applied to prepare hollow nanopowders. For example, the Kirkendall effect, galvanic exchange, and anion exchange, can all result in the void formation of nanopowders.[22–29] Thin-walled, hollow nanopowders composed of transition metal oxides have been successfully applied as anode materials for lithium-ion batteries (LIBs) because of their unique structure, which provides an enhanced surface-to-volume ratio and a reduced transport length for both mass and charge transport.[8–10,20,30–38] These characteristics enable these nanopowders to have superior electrochemical properties such as high specific capacities, fast rate performances, and long cycle lives. In particular, hollow nickel oxide nanopowders that were prepared using liquid solution processes have also been applied as anode materials for LIBs.[20,33–37] For instance, Sasidharan *et al.* prepared nano-sized hollow NiO spheres utilizing a soft-template self-assembly process that used ABC triblock copolymeric micelles.[35] The hollow NiO nanospheres obtained using this procedure performed well as an anode material. Huang *et al.* synthesized hollow NiO spheres by heating a $NiCl_2$/resorcinol-formaldehyde (RF) gel under an argon atmosphere and subsequently, in oxygen.[34] These hollow spheres had a diameter of about 2 μm and were composed of NiO particles that were about 200 nm in diameter. Moreover, they exhibited a good rate capability. The Kirkendall effect has also been applied for the preparation of NiO nanopowders.[25,26,39] Tracy *et al.* observed the transformation of Ni nanoparticles of different sizes (with average diameters of 9, 26, and 96 nm) under oxidation conditions to hollow (single void) or porous (multiple voids) NiO through the nanoscale Kirkendall effect.[25] By choosing an intermediate oxidation temperature and by varying the reaction time, partially oxidized Ni(core)/NiO(shell) NPs could be controllably synthesized.

However, currently, the application of hollow NiO nanopowders is limited due to the difficulties of controlling their preparation and recovering processes. For this reason, complex, hollow NiO structures are highly desirable and can provide more tunability by manipulating the structure of the

Department of Materials Science and Engineering, Korea University, Anam-Dong, Seongbuk-Gu, Seoul 136-713, Republic of Korea. E-mail: yckang@korea.ac.kr; Fax: (+82) 2-928-3584

†Electronic supplementary information (ESI) available. See DOI: 10.1039/c5nr05930e

hollow materials on the micro- and nano-scale. Moreover, aggregates of the hollow nanopowders could exhibit the unique properties of the hollow nanopowders and, as such, could be efficiently applied to various fields, including energy storage.[40–44]

In this study, a method to prepare micron-sized, spherical and hollow-structured NiO aggregates, which exhibit the unique properties of hollow nanopowders, was introduced. In particular, a one-pot spray pyrolysis process that combined the Kirkendall effect with Ostwald ripening was successfully developed. The NiO–C composite powder prepared by one-pot spray pyrolysis was transformed into micron-sized spherical and hollow-structured NiO aggregates through a two-step post-treatment process. The electrochemical properties of the uniquely structured NiO aggregates were compared with those of solid NiO aggregates and hollow NiO shells prepared using the same spray pyrolysis process.

Experimental section

Sample preparation

Spherical and hollow-structured NiO aggregates were prepared using a three-step process. First, a nickel oxide–PVP composite precursor powder was prepared utilizing a spray pyrolysis process with a spray solution that consisted of nickel nitrate hexahydrate [$(Ni(NO_3)_2)\cdot 6H_2O$, Sigma Aldrich] and polyvinylpyrrolidone (PVP) [$(C_6H_9NO)_n$, M_w-40 000, Sigma Aldrich]. In the spray pyrolysis system that was used, droplets were generated using a 1.7 MHz ultrasonic spray generator that consisted of six vibrators. The droplets were carried to a quartz reactor (length = 1200 mm, diameter = 50 mm) using N_2 carrier gas at a flow rate of 10 L min^{-1}. The reactor temperature was maintained at 500 °C. The concentrations of nickel nitrate hexahydrate and PVP that were dissolved in distilled water to prepare the spray solution were 0.1 M and 20 g L^{-1}, respectively. The first stage of the post-treatment process involved heating the nickel oxide–PVP composite powders to 300 °C under a 10% H_2/Ar reducing atmosphere for 10 h to produce metallic Ni–carbon composite powders. The second stage of the post-treatment process involved heating the metallic Ni–carbon composite powders to 300 °C under an oxidizing air atmosphere for 5 h to produce the final aggregates of hollow NiO nanospheres. For comparison purposes, hollow NiO shells were prepared directly with spray pyrolysis using an identical spray solution as described above but without PVP. The droplets were carried to a quartz reactor using air as the carrier gas at a flow rate of 10 L min^{-1}. The reactor temperature was also maintained at 500 °C.

Characterization

The microstructure of the powders was observed using field emission scanning electron microscopy (SEM, Hitachi, S-4800) and field emission transmission electron microscopy (TEM, JEOL, JEM-2100F). In addition, their crystal structures were evaluated through X-ray diffraction (XRD, X'Pert PRO MPD) using Cu K_α radiation (λ = 1.5418 Å) at the Korea Basic Science Institute (Daegu). X-ray photoelectron spectroscopy (XPS, Thermo Scientific K-Alpha), with a focused monochromatic Al Kα at 12 kV and 20 mA, was used to analyze the composition of the specimens. The surface area of the powders was determined using the Brunauer–Emmett–Teller (BET) method, where N_2 was the adsorbate gas. Finally, thermogravimetric analysis (TGA) was performed using a Pyris 1 TGA (Perkin Elmer, temperature range = 25–650 °C, heating rate = 10 °C min^{-1}, static air atmosphere).

Electrochemical measurements

The electrochemical properties of the powders were analyzed by constructing 2032-type coin cells. The anode was prepared by mixing the active material, carbon black, and sodium carboxymethyl cellulose (CMC) in a weight ratio of 7 : 2 : 1. A Li metal and microporous polypropylene film were used as the counter electrode and separator, respectively. The electrolyte was prepared by dissolving 1 M of $LiPF_6$ in a mixture of fluoroethylene carbonate and dimethyl carbonate (FEC/DMC, 1 : 1 v/v). The discharge/charge characteristics of the samples were investigated by cycling over a potential range of 0.001–3 V at various current densities. Cyclic voltammograms were measured at a scan rate of 0.07 mV s^{-1}. The size of the negative electrode containing the NiO powders was 1 cm × 1 cm and the mass loading was approximately 1.2 mg cm^{-2}. Electrochemical impedance spectra were obtained by AC electrochemical impedance spectroscopy (EIS) with a ZIVE SP1 over a frequency range of 0.01 Hz–1000 kHz and at a potential amplitude of 10 mV.

Results and discussion

The characteristics of the powders that were directly prepared using spray pyrolysis, where the spray solution contained Ni nitrate hexahydrate and PVP, are shown in Fig. S1.† The XRD pattern of the powders has small peaks that represent NiO and a broad peak around 25°, which reveals the formation of amorphous carbon. The TG curve shown in Fig. 1Sb† reveals the steep weight loss that occurred at temperatures between 280 and 410 °C. The high weight loss that was observed at temperatures below 410 °C can mainly be attributed to the decomposition of PVP and the combustion of amorphous carbon. The complete conversion of PVP into amorphous carbon did not occur during the spray pyrolysis process due to the short residence time of the powders inside the hot wall reactor, which was maintained at 500 °C. Therefore, the powders shown in Fig. S1c† are the PVP–C–NiO composite. Moreover, the powders shown in Fig. S1c† have a uniform debossed structure. Drying of the droplet, which was several microns in size, produced a PVP–nickel nitrate composite. Melting of nickel nitrate, which has a low melting temperature of 56.7 °C, and PVP resulted in phase separation within the dried powder. In particular, the melted PVP migrated to the surface of the powder during this segregation. Therefore, the drying and partial decomposition of the melted PVP formed a

debossed structure and the decomposition of nickel nitrate into NiO occurred. Consequently, the PVP-rich shell covered the nickel oxide-rich core in the powder.

The debossed structure of the precursor powders that was obtained through spray pyrolysis was maintained after post-treatment at 300 °C under 10% H_2/Ar gas, as shown by SEM and TEM images (Fig. 1a–d). The high-resolution TEM images shown in Fig. 1d reveal that the Ni nanocrystals are embedded within the amorphous carbon matrix. In particular, the carbonization of PVP forms the amorphous carbon matrix. The high-resolution TEM image shown in Fig. 1d shows the single crystalline structure of the nanocrystals and clear lattice fringes that are separated by 0.20 nm, which corresponds to the (111) crystal plane of face-centered cubic (fcc) Ni (JCPDS card no. 04-0850). Moreover, the XRD pattern of the reduced powder exhibits the pure crystalline peaks of metallic Ni (Fig. S2†). The SAED pattern and elemental mapping images shown in Fig. 1e and f, respectively, also suggest the complete reduction of NiO into metallic Ni following the post-treatment process under a reducing atmosphere. The Ni 2p XPS spectrum of the Ni–C composite powder (Fig. S3a†) clearly demonstrates the existence of metallic Ni at 852.9 eV as well as NiO (Ni^{2+} 854.5 eV), which is formed due to the partial surface oxidation of Ni nanocrystals when exposed to air. Finally, the mean size of the metallic Ni nanoclusters observed from the TEM images was 5 nm.

The post-treatment of the Ni–C composite powders at a temperature of 300 °C under an air atmosphere produced NiO powders, which was confirmed from the XRD pattern shown in Fig. S2.† The debossed and spherical morphology of the Ni–C composite powder was well maintained after the post-treatment process, as shown through SEM imaging. However, the TEM image, which is shown in Fig. 1h, reveals different morphologies compared with that of the Ni–C composite powders. The filled-structured Ni–C powder, which has a high density, transforms into hollow-structured NiO aggregates that are characterized by a high porosity. The TEM image shown in Fig. 1i displays the ultrafine NiO nanocrystals and hollow-structured NiO nanopowders, which are indicated by arrows. The ultrafine Ni nanocrystals transform into hollow NiO nanopowders through a well-known nanoscale Kirkendall diffusion process. In particular, the Ni cations diffused outwards more rapidly than the inward diffusion of oxygen. This is consistent with the larger ionic radius of O^{2-} anions (140 pm) when compared to that of Ni cations (Ni^{2+} has a radius of 83 pm). The complete conversion of metallic Ni single nanocrystals into the polycrystalline NiO nanopowder results in the empty voids found within the nanopowder. During the early stages of the

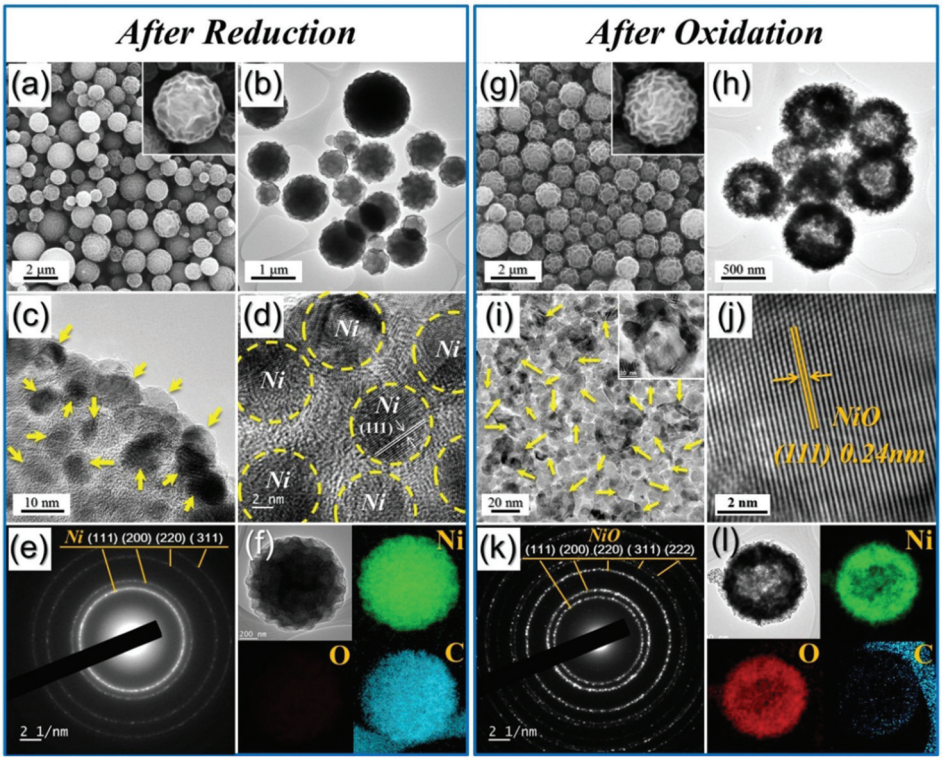

Fig. 1 Morphologies, SAED pattern, and elemental mapping images of (a–f) Ni–C composite powders obtained by reduction of the as-prepared precursor powders at 300 °C under 10% H_2/Ar gas and (g–l) spherical and hollow NiO aggregates obtained by oxidation of reduced Ni–C composite powders at 300 °C under air: (a and g) SEM images, (b, c, h and i) TEM images, (d and j) HR-TEM images, (e and k) SAED patterns, and (f and i) elemental mapping images.

reduction process that is needed to prepare the Ni–C composite powder, metallic Ni nanocrystals were observed to first form around the surface of the Ni–C composite powder. These Ni nanocrystals grow as a result of further reduction through Ostwald ripening. Therefore, the Ni nanocrystals located at the center of the Ni–C composite powder are smaller than those located at the surface. Ostwald ripening also occurs during the nanoscale Kirkendall diffusion process. The ultrafine NiO nanocrystals formed at the center of the powder diffuse towards the outside of the powder by Ostwald ripening.[45–48] Consequently, the filled-structured Ni–C powders transform into the hollow and nanostructured NiO powders through the synergetic effect of nanoscale Kirkendall diffusion and Ostwald ripening. The high-resolution TEM image shown in Fig. 1j shows clear lattice fringes separated by 0.24 nm, which corresponds to the (111) crystal plane of fcc NiO (JCPDS card no. 47-1049). The XPS spectrum of the NiO powder showed only Ni peaks for the oxide, with binding energies of NiO (Ni^{2+} 854.5 eV) and Ni_2O_3 (Ni^{3+} 855.8 eV), as shown in Fig. S3b.† The SAED pattern and elemental mapping images shown in Fig. 1k and l, respectively, also reveal complete conversion of metallic Ni into NiO by oxidation. In particular, the carbon component was scarcely detected in the elemental mapping images. Therefore, complete combustion of amorphous carbon during the oxidation process resulted in pure nanostructured, hollow NiO powders. The TGA curve in Fig. S4b† also reveals the formation of carbon-free NiO powders.

The characteristics of the solid NiO aggregates formed by the direct oxidation of the precursor powders that were obtained through spray pyrolysis are shown in Fig. S5.† The overall morphology of the precursor powders was well maintained even after post-treatment processing at 300 °C. During the oxidation process, complete decomposition of PVP and crystallization of NiO resulted in carbon-free polycrystalline NiO powders that had a filled structure as confirmed by high-resolution TEM, SAED patterns, and elemental mapping images (Fig. S5†). The BET surface areas of the NiO aggregates with solid and hollow structures, are 24 and 23 $m^2\ g^{-1}$, respectively, and their mean crystallite sizes, which were calculated from the half peak width of the (200) crystal plane using the Scherrer equation, are 11 and 10 nm, respectively. The NiO aggregates with solid and hollow structures had well developed mesopores as shown in Fig. S8.† The detailed mechanism of formation for the spherical and hollow-structured NiO aggregates, which was estimated from the morphological changes that occurred during the post-treatment processes, is summarized in Scheme 1.

The hollow NiO shell that was used as a comparison was also prepared using spray pyrolysis. These hollow NiO shells were directly prepared through spray pyrolysis, which occurred under an air atmosphere using a spray solution without PVP, and have hollow and thin-walled structures as shown in Fig. S6.† The high evaporation and decomposition rates of the droplets resulted in the production of the hollow NiO shell. The thin shell of the hollow powder is composed of ultrafine NiO nanocrystals as shown in Fig. S6d.† The SAED and XRD

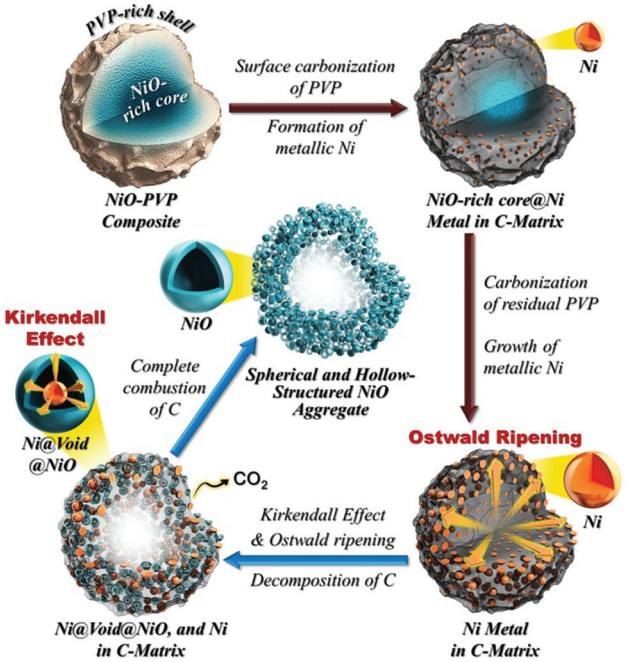

Scheme 1 Schematic diagram for the detailed mechanism of formation for the spherical and hollow-structured NiO aggregate.

patterns and the elemental mapping images shown in Fig. S6d–g† reveal the formation of carbon-free polycrystalline NiO shells. The BET surface area and mean crystallite size of the hollow NiO shell are 18 $m^2\ g^{-1}$ and 20 nm, respectively.

Next, the electrochemical properties of the hollow NiO aggregates, which were formed through the synergetic effects of nanoscale Kirkendall diffusion and Ostwald ripening, were compared to solid NiO aggregates and hollow NiO shells. The cyclic voltammogram (CV) curves of the hollow NiO aggregates for the first five cycles, which had a scan rate of 0.07 mV s^{-1}, are shown in Fig. 2a. An intensive reduction peak centered at 0.42 V corresponds to the formation of a partially reversible solid electrolyte interface (SEI) layer and the initial reduction of NiO to metallic Ni nanoparticles, which occurs according to eqn (1).[49,50]

$$NiO + 2Li^+ + 2e^- \rightarrow Ni + Li_2O \quad (1)$$

An extra shoulder reduction peak at around 0.74 V was observed following the first discharge. The imperfection of the NiO lattice of the hollow and nanostructured NiO powders, which was caused by the low post-treatment temperature of 300 °C, resulted in this extra reduction peak.[51,52] The main reduction peak shifted to a higher potential after the first cycle due to the formation of ultrafine NiO nanocrystals. Two broad oxidation peaks were observed from the first cycle onward at around 1.6 and 2.3 V, respectively, due to the oxidation of Ni nanocrystals to NiO and the subsequent decomposition of the SEI layer.[51–55] This process occurs according to eqn (2).

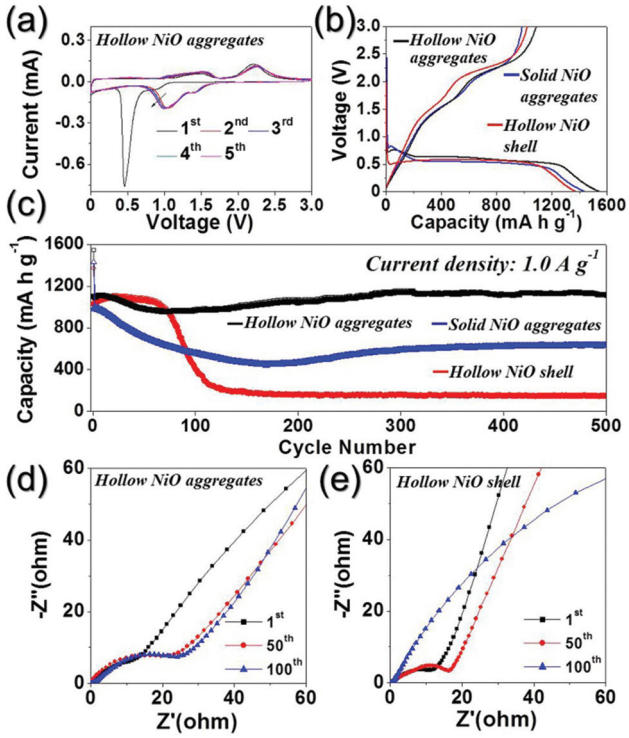

Fig. 2 Electrochemical properties of the hollow NiO aggregates, which were formed through the synergetic effects of nanoscale Kirkendall diffusion and Ostwald ripening, solid NiO aggregates and hollow NiO shells: (a) cyclic voltammogram (CV) curves of the hollow NiO aggregates for the first 5 cycles, (b) initial charge/discharge curves, (c) cycling performances at a constant current density of 1.0 A g^{-1}, (d) Nyquist impedance plots after cycling of the hollow NiO aggregates, and (e) Nyquist impedance plots after cycling of the hollow NiO shell.

$$Ni + Li_2O \leftrightarrow NiO + 2Li^+ + 2e^- \quad (2)$$

The high degree of overlap that occurs in the CV curves beginning from the second cycle reveals the excellent reversible lithium-ion storage performance of the hollow NiO aggregates. The CV curves of the solid NiO aggregates and hollow NiO shells, which are shown in Fig. S9,† are also shaped similarly to those of the hollow and nanostructured NiO aggregates. The initial discharge and charge curves of the three samples, which were measured at a current density of 1 A g^{-1}, are shown in Fig. 2b. The three samples have long plateaus during their first discharge due to the conversion of polycrystalline NiO to metallic Ni, as described in the CV results.

Additionally, short plateaus at around 0.75 V are observed in the first discharge curve of the NiO aggregates with hollow and solid structures that were prepared from the spray solution with PVP. The long-term cycling performances of the three samples at a current density of 1 A g^{-1} are shown in Fig. 2c. Overall, it was found that the hollow NiO aggregates that were formed using the synergetic effects of nanoscale Kirkendall diffusion and Ostwald ripening have superior cycling performance when compared to those of the solid NiO aggregates and hollow NiO shells. In particular, the hollow NiO shell that was prepared directly by spray pyrolysis, wherein the spray solution lacked PVP, had good cycling performance during the first 60 cycles. However, thereafter, their discharge capacities suddenly dropped to 186 mA h g^{-1} for the 140th cycle. On the other hand, the discharge capacities of the solid NiO aggregates, which were prepared from a spray solution containing PVP, dropped continuously to 453 mA h g^{-1} by the 170th cycle. The discharge capacity of the hollow NiO aggregates, which were formed using the synergetic effect of nanoscale Kirkendall diffusion and Ostwald ripening, was 1118 mA h g^{-1} for the 500th cycle and their capacity retention measured from the second cycle was almost 100%. However, the discharge capacities of the solid NiO aggregates and hollow NiO shells, which were prepared from the spray solutions with and without PVP, were 631 and 150 mA h g^{-1}, respectively, for the 500th cycle and their capacity retentions measured from the second cycle were only 63 and 14%, respectively.

Electrochemical impedance spectroscopy (EIS) measurements of the three samples were taken before and after cycling to investigate the superior lithium-ion storage properties of the spherical and hollow NiO aggregates that were formed using the synergetic effect of nanoscale Kirkendall diffusion and Ostwald ripening. The Nyquist plots that are shown in Fig. 2d, e and S10† reveal compressed semicircles in the medium-frequency range, which describe the charge-transfer resistance (R_{ct}) of the electrode.[56–58] The thin-walled, hollow NiO shell prepared directly by spray pyrolysis from a spray solution lacking PVP had the lowest charge-transfer resistance before cycling (Fig. S10a†), which was due to the high contact area between the NiO crystals and the liquid electrolyte. The charge-transfer resistances of the three samples were found to abruptly decrease after the first cycling due to the formation of ultrafine nanocrystals. The charge-transfer resistances of the hollow NiO aggregates, which were formed using the synergetic effect of nanoscale Kirkendall diffusion and Ostwald ripening, increased due to the partial structural destruction that occurs during the first 50 cycles (Fig. 2d). However, the low charge-transfer resistance of the electrode was maintained for another 50 cycles. The low charge-transfer resistances of the thin-walled, hollow NiO shell prepared directly by spray pyrolysis were also observed for the first 50 cycles (Fig. 2e). However, the Nyquist plot shown in Fig. 2e reveals the high charge-transfer resistance of the thin-walled hollow NiO shell for the 100th cycle. The Nyquist plots shown in Fig. S10b† were obtained using the solid NiO aggregates that were prepared from a spray solution containing PVP. In particular, these results reveal a continuous increase in the charge-transfer resistances over 100 cycles.

The morphologies of the three samples obtained after 500 cycles are shown in Fig. 3. The structural destruction of the solid NiO aggregates and hollow NiO shells, which were prepared from spray solutions with and without PVP, that occurred during repeated lithium insertion and desertion was found to increase their charge-transfer resistances. However, the spherical and hollow NiO aggregates that were formed using the synergetic effect of nanoscale Kirkendall diffusion

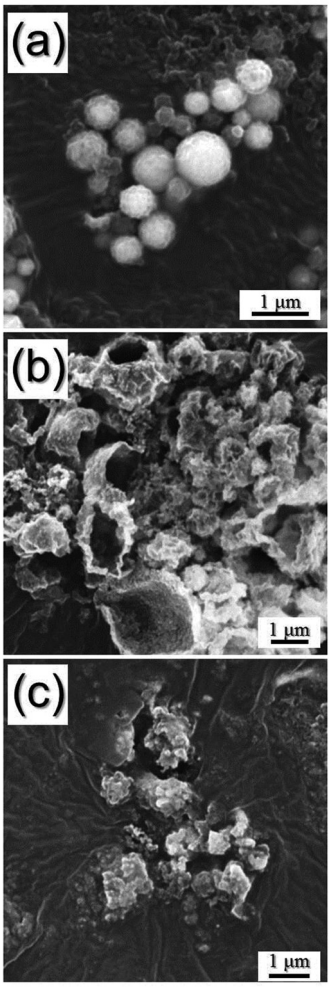

Fig. 3 Morphologies of the NiO powders obtained after 500 cycles: (a) hollow NiO aggregates, (b) hollow NiO shells, and (c) solid NiO aggregates.

and Ostwald ripening had high structural stability during cycling and, as such, had excellent lithium storage properties.

Conclusions

The synthesis of spherical and hollow-structured NiO aggregates using the synergetic effect of nanoscale Kirkendall diffusion and Ostwald ripening was introduced. The precursor powders were prepared using one-pot spray pyrolysis and were then transformed into spherical and hollow-structured NiO aggregates using a simple two-step post-treatment process. Nanoscale Kirkendall diffusion and Ostwald ripening occurred during the two-step post-treatment process, which used reducing and oxidizing atmospheres. The spherical and hollow-structured NiO aggregates had high structural stability during repeated lithium insertion and desertion due to their unique structure and showed superior electrochemical properties when compared with those of solid NiO aggregates and hollow NiO shells prepared using the same spray pyrolysis process.

Acknowledgements

This work is supported by the National Research Foundation of Korea (NRF) grant funded by the Korea Government (MEST) (no. 2013R1A2A1A01006545).

Notes and references

1 X. Lai, J. Li, B. A. Korgel, Z. Dong, Z. Li, F. Su, J. Du and D. Wang, *Angew. Chem., Int. Ed.*, 2011, **123**, 2790–2793.
2 Z. Ai, Z. Gao, L. Zhang, W. He and J. J. Yin, *Environ. Sci. Technol.*, 2013, **47**, 5344–5352.
3 B. Wang, J. S. Chen, H. B. Wu, Z. Wang and X. W. Lou, *J. Am. Chem. Soc.*, 2011, **133**, 17146–17148.
4 J. Wang, N. Yang, H. Tang, Z. Dong, Q. Jin, M. Yang, D. Kisailus, H. Zhao, Z. Tang and D. Wang, *Angew. Chem., Int. Ed.*, 2013, **125**, 6545–6548.
5 Z. Wang, L. Zhou and X. W. Lou, *Adv. Mater.*, 2012, **24**, 1903–1911.
6 H. B. Wu, J. S. Chen, H. H. Hng and X. W. Lou, *Nanoscale*, 2012, **4**, 2526–2542.
7 M. Zhen, X. Guo, G. Gao, Z. Zhou and L. Liu, *Chem. Commun.*, 2014, **50**, 11915–11918.
8 C. Niu, J. Meng, C. Han, K. Zhao, M. Yan and L. Mai, *Nano Lett.*, 2014, **14**, 2873–2878.
9 L. Zhou, H. Xu, H. Zhang, J. Yang, S. B. Hartono, K. Qian, J. Zou and C. Yu, *Chem. Commun.*, 2013, **49**, 8695–8697.
10 X. Zhou, Y. X. Yin, L. J. Wan and Y. G. Guo, *J. Mater. Chem.*, 2012, **22**, 17456–17459.
11 X. W. Lou, L. A. Archer and Z. Yang, *Adv. Mater.*, 2008, **20**, 3987–4019.
12 Y. Zhong, L. Su, M. Yang, J. Wei and Z. Zhou, *ACS Appl. Mater. Interfaces*, 2013, **5**, 11212–11217.
13 X. H. Xia, J. P. Tu, X. L. Wang, C. D. Gu and X. B. Zhao, *Chem. Commun.*, 2011, **47**, 5786–5788.
14 G. Li, X. Wang, L. Liu, R. Liu, F. Shen, Z. Cui, W. Chen and T. Zhang, *Small*, 2015, **11**, 731–739.
15 X. Tong, Y. Qin, X. Guo, O. Moutanabbir, X. Ao, E. Pippel, L. Zhang and M. Knez, *Small*, 2012, **8**, 3390–3395.
16 J. Ning, G. Xiao, L. Wang, B. Zou, B. Liu and G. Zou, *Nanoscale*, 2011, **3**, 741–745.
17 G. Xiao, C. Zhu, Y. Ma, B. Liu, G. Zou and B. Zou, *Angew. Chem., Int. Ed.*, 2014, **126**, 748–752.
18 K. An and T. Hyeon, *Nano Today*, 2009, **4**, 359–373.
19 J. Hu, M. Chen, X. Fang and L. Wu, *Chem. Soc. Rev.*, 2011, **40**, 5472–5491.
20 X. Lai, J. E. Halpert and D. Wang, *Energy Environ. Sci.*, 2012, **5**, 5604–5618.
21 Q. Zhang, W. Wang, J. Goebl and Y. Yin, *Nano Today*, 2009, **4**, 494–507.
22 J. S. Cho, Y. J. Hong and Y. C. Kang, *ACS Nano*, 2015, **9**, 4026–4035.
23 J. S. Cho, Y. J. Hong, J. H. Lee and Y. C. Kang, *Nanoscale*, 2015, **7**, 8361–8367.

24 W. Wang, J. Goebl, L. He, S. Aloni, Y. Hu, L. Zhen and Y. Yin, *J. Am. Chem. Soc.*, 2010, **132**, 17316–17324.
25 B. D. Anderson and J. B. Tracy, *Nanoscale*, 2014, **6**, 12195–12216.
26 J. G. Railsback, A. C. Johnston-Peck, J. Wang and J. B. Tracy, *ACS Nano*, 2010, **4**, 1913–1920.
27 G. Gao, L. Yu and H. B. Wu, *Small*, 2014, **10**, 1741–1745.
28 G. Xiao, Y. Zeng, Y. Jiang, J. Ning, W. Zheng, B. Liu, X. Chen, G. Zou and B. Zou, *Small*, 2013, **9**, 793–799.
29 Y. Yin, R. M. Rioux, C. K. Erdonmez, S. Hughes, G. A. Somorjai and A. P. Alivisatos, *Science*, 2004, **304**, 711–714.
30 B. Koo, H. Xiong, M. D. Slater, V. B. Prakapenka, M. Balasubramanian, P. Podsiadlo, C. S. Johnson, T. Rajh and E. V. Shevchenko, *Nano Lett.*, 2012, **12**, 2429–2435.
31 X. Wang, X. L. Wu, Y. G. Guo, Y. Zhong, X. Cao, Y. Ma and J. Yao, *Adv. Funct. Mater.*, 2010, **20**, 1680–1686.
32 M. Xu, L. Kong, W. Zhou and H. Li, *J. Phys. Chem. C*, 2007, **111**, 19141–19147.
33 C. Y. Cao, W. Guo, Z. M. Cui, W. G. Song and W. Cai, *J. Mater. Chem.*, 2011, **21**, 3204–3209.
34 X. H. Huang, J. P. Tu, C. Q. Zhang and F. Zhou, *Electrochim. Acta*, 2010, **55**, 8981–8985.
35 M. Sasidharan, N. Gunawardhana, C. Senthil and M. Yoshio, *J. Mater. Chem. A*, 2014, **2**, 7337–7344.
36 D. Xie, W. Yuan, Z. Dong, Q. Su, J. Zhang and G. Du, *Electrochim. Acta*, 2013, **92**, 87–92.
37 C. Zhong, J. Z. Wang, S. L. Chou, K. Konstantinov, M. Rahman and H. K. Liu, *J. Appl. Electrochem.*, 2010, **40**, 1415–1419.
38 J. Zhu, Z. Yin, D. Yang, T. Sun, H. Yu, H. E. Hoster, H. H. Hng, H. Zhang and Q. Yan, *Energy Environ. Sci.*, 2013, **6**, 987–993.
39 W. Wang, M. Dahl and Y. Yin, *Chem. Mater.*, 2013, **25**, 1179–1189.
40 D. Chen, G. Ji, Y. Ma, J. Y. Lee and J. Lu, *ACS Appl. Mater. Interfaces*, 2011, **3**, 3078–3083.
41 D. Deng and J. Y. Lee, *Chem. Mater.*, 2008, **20**, 1841–1846.
42 H. Guo, R. Mao, D. Tian, W. Wang, D. Zhao, X. Yang and S. Wang, *J. Mater. Chem. A*, 2013, **1**, 3652–3658.
43 K. Hadinoto, P. Phanapavudhikul, Z. Kewu and R. B. Tan, *Ind. Eng. Chem. Res.*, 2006, **45**, 3697–3706.
44 Z. Liu, D. D. Sun, P. Guo and J. O. Leckie, *Chem. – Eur. J*, 2007, **13**, 1851–1855.
45 W. S. Wang, L. Zhen, C. Y. Xu, W. Z. Shao and Z. L. Chen, *CrystEngComm*, 2013, **15**, 8014–8021.
46 W. S. Wang, L. Zhen, C. Y. Xu, B. Y. Zhang and W. Z. Shao, *J. Phys. Chem. B*, 2006, **110**, 23154–23158.
47 J. S. Chen, L. A. Archer and X. W. Lou, *J. Mater. Chem.*, 2011, **21**, 9912–9924.
48 H. J. Song, X. H. Jia, H. Qi, X. F. Yang, H. Tang and C. Y. Min, *J. Mater. Chem.*, 2012, **22**, 3508–3516.
49 P. Poizot, S. Laruelle, S. Grugeon, L. Dupont and J. M. Tarascon, *Nature*, 2000, **407**, 496–499.
50 J. H. Pan, Q. Huang, Z. Y. Koh, D. Neo, X. Z. Wang and Q. Wang, *ACS Appl. Mater. Interfaces*, 2013, **5**, 6292–6299.
51 B. Varghese, M. V. Reddy, Z. Yanwu, C. S. Lit, T. C. Hoong, G. V. Subba Rao, B. V. R. Chowdari, A. T. S. Wee, C. T. Lim and C. H. Sow, *Chem. Mater.*, 2008, **20**, 3360–3367.
52 H. Liu, G. Wang, J. Liu, S. Qiao and H. Ahn, *J. Mater. Chem.*, 2011, **21**, 3046–3052.
53 Y. K. Sun, M. J. Lee, C. S. Yoon, J. Hassoun, K. Amine and B. Scrosati, *Adv. Mater.*, 2012, **24**, 1192–1196.
54 N. Wang, L. Chen, X. Ma, J. Yue, F. Niu, H. Xu, J. Yang and Y. Qian, *J. Mater. Chem. A*, 2014, **2**, 16847–16850.
55 H. Wu, M. Xu, H. Wu, J. Xu, Y. Wang, Z. Peng and G. Zheng, *J. Mater. Chem.*, 2012, **22**, 19821–19825.
56 J. S. Cho and Y. C. Kang, *Small*, 2015, **11**, 4673–4681.
57 Y. J. Hong, M. Y. Son and Y. C. Kang, *Adv. Mater.*, 2013, **25**, 2279–2283.
58 N. Li, G. Liu, C. Zhen, F. Li, L. Zhang and H. M. Cheng, *Adv. Funct. Mater.*, 2011, **21**, 1717–1722.